DOE/METC-94/1009
(DE94012262)
Distribution Category UC-104

Aerovalve Pulse Combustion

Technical Note

George A. Richards
Randall S. Gemmen
Lakshmanan Narayanaswami

U.S. Department of Energy
Office of Fossil Energy
Morgantown Energy Technology Center
P.O. Box 880
Morgantown, West Virginia 26507-0880

July 1994

DISCLAIMER

Contents

		Page
Executive Summary		1
1	Introduction	2
2	Model Development and Mixing Effects	3
2.1	Model Development	3
2.2	Conservation Laws Within the Combustion Zone	4
2.3	Conservation Laws Within the Inlet and Tailpipe Regions	8
2.4	Solution of the Governing Equations	10
2.5	Mixing Model	10
2.6	Simulation Results - Effect of the Mixing Process	11
3	Experimental and Model Results	16
3.1	Experimental and Model Parameters	16
3.2	Experimental Description	17
3.3	Comparison of Experimental and Numeric Results	19
3.4	Effect of Combustor Geometry	21
3.5	Geometric Configurations for Pressure Gain	24
4	Summary and Conclusions	27
5	Nomenclature	29
6	References	32

List of Figures

Figure		Page
1	Schematic of Processes Occurring in an Aerovalve Pulse Combustor	3
2	Representation of Transport Processes Occurring as the g-Region Mixes With the h-Region	6
3	The Two-Step Mixing Process, Alternating Between the Fast and Slow Mixing Rates	11
4	Effect of the Eddy Time, With t_Δ = 0.01 ms	12
5	Effect of the Eddy Time, With $\tau_{m,f}$ = 0.01 ms	13
6	Time History of Various Parameters for Case (C) in Figure 5	14
7	Time History of Various Parameters for Case (D) in Figure 5	14

List of Figures
(Continued)

		Page
8	Time History for Various Parameters, With Mixing Time Scales $\tau_{m,s}$ = 100 ms, $\tau_{m,f}$ = 30 ms, and t_{Δ} = 2 ms	15
9	Schematic of an Aerovalve Pulse Combustor	16
10	Experimental Pulse Combustor	18
11	Typical Pulse Combustor Pressure Signal	19
12	Comparison of Laboratory Data and Model Predictions for Frequency, Oscillating Pressure Amplitude, and Pressure Differences	21
13	Comparison of the Laboratory Pressure Signal (A) to Model Predictions for Several Different Values of the Mixing Parameters (B) - (F)	22
14	Laboratory Data and Model Predictions for Frequency and RMS Pressure as a Function of Inlet Length	22
15	Model Predictions (a) and Laboratory Data (b) for Pressure Difference as a Function of Inlet Length	23
16	Model Predictions of Inlet and Tailpipe Gas Velocities for the Inlet Lengths of 10 and 30 cm	24
17	Inlet-Combustor Pressure Difference for the Scaled Combustor Geometry Listed in Table 3	25

List of Tables

Table		Page
1	Model Base-Case Parameters	11
2	Dimensions of the Base-Case Combustor	19
3	Dimensions of the Pressure-Gain Combustor	25

Executive Summary

We present a mathematical model and an experimental investigation of aerodynamically valved pulse combustion. The model uses a control-volume approach to solve conservation laws in several regions of a pulse combustor. Combustion is modelled as a bimolecular reaction. Mixing between the fresh charge and combustion products is modelled as a two-step process, with the mixing occurring slowly for a specified eddy time during each cycle, and then changing to a higher rate.

Results of model simulations demonstrate that eddy time plays a significant role in determining the frequency and amplitude of combustion oscillation. We show that short eddy times produce steady, rather than pulsating, combustion. And we show that changes to the mixing process alter the temperature-species history of combustion gases in a manner that could prevent or promote the formation of nitrogen oxides, depending on specific mixing rates.

The relatively simple control-volume approach used in this model allows rapid investigation of a wide range of geometric and operating parameters, and also defines characteristic length and time scales relevant to aerovalve pulse combustion.

Experimental measurements compare favorably to model predictions, based on a control-volume analysis of the pulse combustor. We place particular emphasis on time-averaged pressure differences through the combustor, which act as an indicator of "pressure gain" performance. We investigate both operating conditions and combustor geometry, and we show that a complex interaction between the inlet and exit flows of a combustor makes it difficult to produce general correlations among the various parameters. We use a scaling rule, developed from the control-volume model, to produce a combustor geometry capable of producing pressure gain.

1 Introduction

Pulse combustion has been commercially accepted in the residential heating market for more than a decade [1], and has been used on larger-scale heating devices such as boilers within the last 5 years [2]. New applications of pulse combustion technology continue to emerge for drying, waste disposal, and energy recovery [3]. Pulse combustion enhances the transport of heat or mass and may produce lower pollutant levels than a conventional combustor [4]. Pulse combustors have also been proposed for use in gas turbines [5]; recent work by Kentfield demonstrated that the cycle efficiency of a small gas turbine can be improved using pulsating, rather than steady, combustion [6].

The acoustic resonances in a pulse combustor serve to draw combustion air from the ambient surroundings, and combustion occurs (approximately) as a constant volume process, creating a higher than ambient pressure. Combustion gases are then expelled at high velocity. Given suitable geometrics, this process effectively pumps air from the inlet of the combustor to the exit. The result is an increase in the stagnation pressure of the combustion gases, hence the name "pressure-gain" combustion. In a gas turbine, pressure-gain would actually contribute to compression of the turbine air, reducing the work supplied to the compressor and yielding a consequent increase in cycle efficiency. Combined with the prospect of lower pollutant emissions, this enhanced cycle efficiency is the reason for current interest in the pressure-gain process.

Pulse combustors may be classified into two broad categories: mechanically-valved, and aerodynamically-valved (or, aerovalved). Since the aerovalve combustor has no moving parts, it may be better suited to industrial applications, and in particular the gas turbine. However, there have been few detailed studies of aerovalve combustor design, and there is even less guidance on the optimum method to produce pressure-gain. Kentfield's successful demonstration of the pressure-gain gas turbine concept [6] was based partly on an empirical combustor design, with some analytic work conducted to optimize combustor geometry [7].

Section 2 of this report describes a theoretical model of aerovalve pulse combustion. Section 3 compares the predictions of this model to laboratory measurements, reporting the effect of variations in combustor geometry, flow rate, and other parameters. We use the model to investigate the effect of the mixing process on combustor performance. This mixing process is difficult to quantify in the lab and even more difficult to control. While Section 2 shows that overall combustor performance is dramatically affected by mixing rate, comparison with experimental data (Section 3) shows that a single choice for mixing parameters allows successful simulation over a reasonable range of operating and geometric conditions.

The model is partly based on the success of an earlier numeric simulation of "thermal" pulse combustion [8]. The approach is essentially a control volume formulation for all the relevant conservation laws. This relatively simple approach allows rapid investigation of geometric and operational parameters as well as changes in the combustion mixing process.

2 Model Development and Mixing Effects

2.1 Model Development

A schematic of the processes occurring in a single-pulse combustor cycle is shown in Figure 1. For reference, stations u, i, e, and d are identified as the upstream, inlet, exit, and downstream locations. We define the combustion zone as the region between stations i and e, and assume that combustion occurs only in this region. However, the equations can be modified to allow combustion in the inlet and tailpipe regions as well. Figure 1a shows air may be either drawn in or driven out through both the inlet pipe and the tailpipe. We assume that the fresh air is separated from the combustion gases by a contact surface that moves through the tailpipe and inlet regions. The combustion gases, shown as shaded regions in the figure, are composed of fuel, air, and combustion products. Within the combustion zone, fuel and oxygen react at a rate determined by a one-step Arrhenius kinetic mechanism, described below. Gaseous fuel is supplied to the shaded region in the combustion zone at a fixed rate, $\dot{m}_f$.

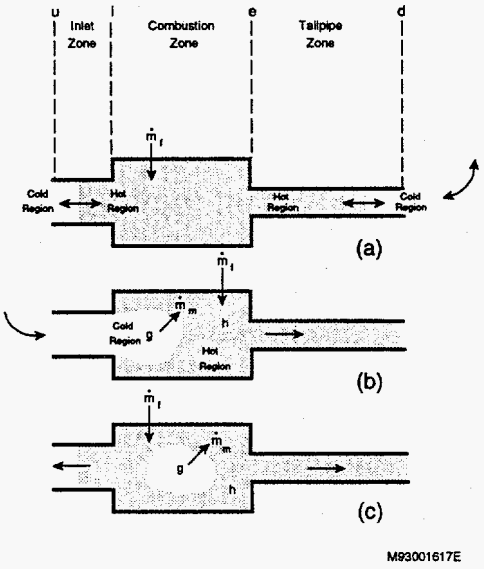

Figure 1. Schematic of Processes Occurring in an Aerovalve Pulse Combustor

Figure 1b represents the induction of fresh air into the combustion zone. The fresh air is mixed with combustion gases at some finite rate, $\dot{m}_m$. If $\dot{m}_m$ is small compared to the rate at which gases enter through station i, a pocket of fresh air will form within the combustor. This pocket is shown schematically as a single region, but the development used here is general enough to cover multiple gas parcels within the combustor. For reference, the pocket of fresh air within the combustion zone is labeled as the g-region, and the hot gases within the combustion zone are denoted as the hot region, or h-region. The g and h regions extend only to stations i and e; they do not include gases within the inlet or tailpipe region.

As air is mixed into the h-region, the combustion reaction raises the temperature of the h-region and produces a concomitant pressure rise in both the g and h regions. Both the g and h regions are characterized by the same uniform pressure, P. As the pressure rises, the inlet flow will reverse, as shown in Figure 1c. At this point, we assume that gases leaving through station i are drawn from the h-region, while any remaining g-region gas continues to mix into the combustion gases.

Control volume conservation laws are developed for each of the various regions. The development that follows is similar to one proposed by Richards et al. [8]. Similar assumptions are used here, including constant specific heat, ideal gas behavior, and uniform conditions within each region. The development is based on the integral form of the conservation laws as presented in most texts [9] and in reference [8]. Assuming uniform conditions within each region, the volume and surface integrals are reduced to algebraic expressions, resulting in a set of first-order differential equations.

2.2 Conservation Laws Within the Combustion Zone

We developed the conservation of energy equation for the combined g and h regions by accounting for the inlet, fuel, and exit flows, $\dot{m}_i$, $\dot{m}_f$, and $\dot{m}_e$, respectively. The heat release per unit volume is **Q** in the h-region, and heat loss occurs by convection through a convection coefficient, **h**, to the combustion zone walls with surface area, A_s, at some specified temperature, T_w. Ideal gas law relations imply $P=(\gamma-1)\rho e$, and assuming that the pressure is constant throughout the combustion zone, the energy balance for the combined g and h regions is

$$\frac{V_c}{\gamma-1}\frac{dP}{dt} = \dot{m}_i C_p T_{oi} + \dot{m}_f C_{pf} T_{of} - \dot{m}_e C_p T_{oe} + \dot{Q} V_h - h A_s (T_h - T_w). \tag{1}$$

The ratio of specific heats, γ, represents an average for the properties of air and combustion products. Equation (1) is normalized by dividing by the ambient pressure, P_A, and the combustion zone volume, V_c. See the nomenclature for the identity of other terms. Denoting normalized values with an overbar, modest algebraic manipulation leads to

$$\frac{d\overline{P}}{dt} = \gamma\left[\frac{\overline{T}_{oi}}{\tau_i} + \frac{\overline{T}_{of}}{\tau_f}\frac{C_{pf}}{C_p} - \frac{\overline{T}_{oe}}{\tau_e}\right] + \frac{\overline{V}_h}{\tau_c} + \frac{(\gamma-1)}{\tau_{HT}}(\overline{T}_w - \overline{T}_h). \tag{2}$$

The characteristic times appearing in equation (2) are defined in equations (3) through (7):

$$\tau_i = \frac{\rho_A V_c}{\dot{m}_i} \quad \textbf{inlet flow time}, \tag{3}$$

$$\tau_f = \frac{\rho_A V_c}{\dot{m}_f} \quad \textbf{fuel flow time}, \tag{4}$$

$$\tau_e = \frac{\rho_A V_c}{\dot{m}_e} \quad \textbf{exit flow time}, \tag{5}$$

$$\tau_c = \frac{P_A}{\dot{Q}\,(\gamma - 1)} \quad \textbf{combustion time, and} \tag{6}$$

$$\tau_{HT} = \frac{\rho_A R V_c}{h A_s} \quad \textbf{heat transfer time.} \tag{7}$$

The reciprocals of these time scales enter into equation (2) and represent rates for the various processes. τ_i, τ_e, and τ_c are not constants, but are calculated from other equations presented later. The inlet and exit flow times have negative values when the flow reverses in either the inlet or tailpipe; i.e., when the flow is moving from right to left at station i or station e.

We use a similar approach to express conservation of mass in the combined g and h regions. The result is

$$\frac{d\bar{\rho}}{dt} = \frac{1}{\tau_i} + \frac{1}{\tau_f} - \frac{1}{\tau_e}. \tag{8}$$

Next we consider conservation laws for the g region alone. As we noted in describing Figure 1, we assume that reverse inlet flow draws mass from the h region. Thus, it is convenient to identify a unit step function, **F**, which is equal to one if the inlet flow is positive (to the right), and zero if the inlet flow is negative (to the left):

$$F = \begin{cases} 1 \text{ when the inlet flow velocity is positive (or zero)} \\ 0 \text{ when the inlet flow velocity is negative} \end{cases} \tag{9}$$

Mass conservation for the g-region is thus expressed as

$$\frac{d}{dt}\left(\bar{\rho}_g \bar{V}_g\right) = F\frac{1}{\tau_i} - \frac{1}{\tau_m}. \tag{10}$$

We identify a mixing time similar to equations (3) through (5) as

$$\tau_m = \frac{\rho_A V_c}{\dot{m}_m}. \tag{11}$$

Energy conservation in the g-region must account for simultaneous transport of enthalpy across station i and across the g-h interface as well as for compression work done on the g-volume. To calculate compression work (i.e., **P dv**), volume changes that are the

genuine result of compression of the g region must be distinguishable from those that result from mixing parcels of g-gases into the h-region. The balance equation is easily derived by treating the combined processes as shown schematically in Figure 2.

The two regions are separated by a contact surface that can move to the left or right. Mixing proceeds from the g to the h region at some specified rate, $\dot{m}_m$. In the absence of changing pressure and with no flow at stations i or e, the contact surface will move from the right to left, performing compression work on the g region, which will exactly equal the flow work associated with the internal energy transported at rate $\dot{m}_m$.

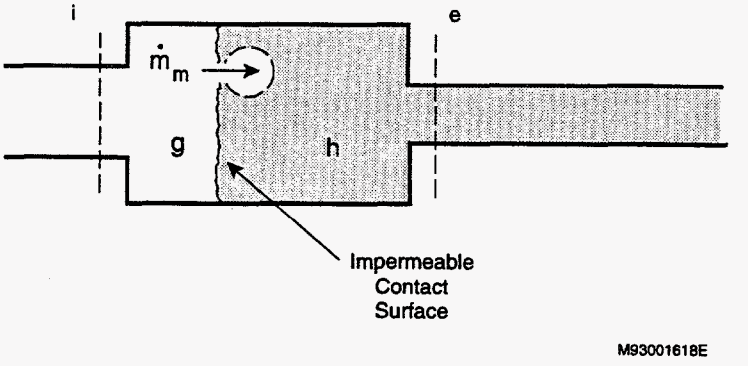

Figure 2. Representation of Transport Processes Occurring as the g-Region Mixes With the h-Region

The balance equation for energy in the g region is thus

$$\frac{d}{dt}\left(\rho_g e_g V_g\right) = F\,\dot{m}_i C_p T_{oi} - \dot{m}_m C_p T_g - P\frac{dV_g}{dt}. \tag{12}$$

The variable **F** defined by equation (9) is again used to distinguish forward and reverse inlet flow. Normalizing the variables, equation (12) becomes

$$\frac{d}{dt}\left(\overline{P}\overline{V}_g\right) = F\,\frac{\gamma}{\tau_i}\,\overline{T}_{oi} - \frac{\gamma}{\tau_m}\,\overline{T}_g - (\gamma-1)\,\overline{P}\,\frac{d}{dt}\,\overline{V}_g. \tag{13}$$

Performing the derivative on the left side, and solving for the derivative of the g-volume, equation (13) becomes

$$\frac{d}{dt}\left(\overline{P}\overline{V}_g\right) = F\,\frac{\overline{T}_{oi}}{\tau_i} - \frac{\overline{T}_g}{\tau_m} + \frac{\gamma-1}{\gamma}\,\overline{V}_g\,\frac{d\overline{P}}{dt}. \tag{14}$$

A total of seven variables must be determined to specify the state of the system: the pressure (the same for both g and h regions) and the density, temperature, and volume for each of the two regions. Equations (2), (8), (10), and (14) represent mass and energy conservation for the combustion zone and the g region alone, providing four of the needed relations. The remaining three equations needed to calculate system behavior are the ideal gas law and some obvious relationships between the volume and density of each region:

$$\overline{P} = \overline{\rho}_j \overline{T}_j \quad ; \quad j = g \text{ or } h, \tag{15}$$

$$\overline{V}_g + \overline{V}_h = 1, \text{ and} \tag{16}$$

$$\overline{\rho}_g \overline{V}_g + \overline{\rho}_h \overline{V}_h = \overline{\rho}. \tag{17}$$

We still need an expression for combustion time. Combustion time is determined from an Arrhenius rate law for the bi-molecular reaction of fuel and oxygen in the h-region. The form of this rate law and the specific rate constants are taken from Kretschmer and Odgers [10]. After considerable algebraic manipulation of their rate law, the combustion time is

$$[\tau_c]^{-1} = K\,(\gamma - 1)\left(\frac{P_A}{P_{STD}}\right)\left(\frac{T_{STD}^{0.5}}{T_A^{1.5}}\right)\frac{\Delta H_f}{R}\,\overline{P}^2\,\overline{T}_h^{-1.5}\,Y_{ox}\,Y_f \exp\left(-\overline{T}_{act}/\overline{T}_h\right). \tag{18}$$

Values for the various constants are listed in the nomenclature. P_{STD} and T_{STD} represent the standard conditions 101 kPa and 300 K. The ambient conditions P_A and T_A represent conditions of the air supplied to the combustor.

Calculation of the combustion time requires the fuel and oxygen mass fractions. Conservation laws for species are developed in a manner similar to other balance equations already presented. Balance equations are thus written for the fuel and oxygen in the h region, but the form of these equations is different when the g region is present. To account for this difference, it is convenient to identify **G** as a unit step function that has a value of one when the g region exists and zero when it is absent:

$$G = \begin{cases} 1 \text{ when the g-region is present} \\ 0 \text{ when the g-region is absent} \end{cases} \tag{19}$$

Employing the same normalization as used before, the balance equations for fuel and oxygen species in the h region are

$$\frac{d}{dt}\left(\overline{\rho}_h Y_{fh} \overline{V}_h\right) = \frac{1}{\tau_f} + Y_{fh}\left[-\frac{1}{\tau_e} + \frac{1}{\tau_i}(1 - F)\right] - \frac{C_V T_A}{\Delta H_f}\frac{\overline{V}_h}{\tau_c}, \text{ and} \tag{20}$$

$$\frac{d}{dt}\left(\overline{\rho}_h Y_{ox,h} \overline{V}_h\right) = Y_{ox,A}\frac{G}{\tau_m} + Y_{ox,i}\frac{1 - GF}{\tau_i} - Y_{ox,h}\frac{1}{\tau_e} - \frac{C_V T_A}{\Delta H_f}\frac{\overline{V}_h}{\tau_c} S_R. \tag{21}$$

2.3 Conservation Laws Within the Inlet and Tailpipe Regions

The tailpipe and inlet equations are essentially identical in form and are described below for only the inlet. Analogous expressions apply to the tailpipe, except as noted.

The gases within the inlet are treated as a slug flow with velocity **u**. A contact surface may exist within the inlet when fresh air is drawn from the ambient surroundings (Figure 1a) and flows to station i. To normalize, we identify a reference inlet length, L_{ri}, as the ratio of the combustor volume and the inlet cross-sectional area (see the nomenclature, Section 5). Also, we define a reference velocity, u_r, is defined as $\sqrt{RT_a}$. Then, letting $\bar{L}_a$ denote the normalized length between station u and the contact surface, the contact surface motion is tracked by the obvious kinematic relations:

$$\frac{d\bar{L}_a}{dt} = \frac{\bar{u}}{\tau_{ri}} \quad , \quad \text{and} \quad \bar{L}_b = \bar{L}_i - \bar{L}_a , \tag{22}$$

where τ_{ri} is a reference time for inlet processes, defined in the nomenclature. The regions on either side of the contact surface are characterized by a single value for all properties. The subscript **a** corresponds to gases drawn from ambient conditions and the subscript **b** indicates properties of the burned gas region. The combustion reaction is assumed to be quenched in the burned region, but fuel and oxygen are otherwise tracked. Using the **a** and **b** subscripts, conservation of mass in the ambient and burned regions takes the following form:

$$\frac{d\bar{\rho}_a}{dt} = \frac{\bar{\rho}_u - \bar{\rho}_a}{\tau_{ri}} \frac{\bar{u}}{\bar{L}_a} , \text{ and} \tag{23}$$

$$\frac{d\bar{\rho}_b}{dt} = \frac{\bar{\rho}_b - \bar{\rho}_i}{\tau_{ri}} \frac{\bar{u}}{\bar{L}_b} . \tag{24}$$

Next, we define a momentum balance equation for the combined ambient and burned regions. This equation balances the change of momentum for both regions, and the corresponding friction and pressure forces act on the slug of fluid. The friction forces are calculated from the wall shear stresses, $\bar{S}_a$ and $\bar{S}_b$ (normalized by the ambient pressure), times the surface areas, A_{sa} and A_{sb}, in each region. These stresses are calculated using a conventional friction coefficient, **f**, as defined by Schlichting [11]. Algebraic manipulation of equations (22) through (24) yields the momentum balance as

$$\left(\bar{\rho}_a \bar{L}_a + \bar{\rho}_b \bar{L}_b\right) \frac{d\bar{u}}{dt} = \frac{\bar{P}_u - \bar{P}_i}{\tau_{ri}} - \frac{\bar{S}_a A_{sa} + \bar{S}_b A_{sb}}{\tau_{ri} A_i} . \tag{25}$$

We then write an individual energy balance for the ambient and burned regions. The energy balance for these regions must account for pressure forces that perform work on each end of the fluid regions, **a** and **b**. The pressure at stations i and e are determined from the boundary conditions described below. We calculate the pressure at the contact surface from a momentum balance that is applied to regions **a** and **b** ***individually***, as opposed to the overall momentum balance for both regions, equation (25). Using the resulting expression for the contact surface pressure, and combining the expression with equations (22) through (24), the energy balance for each region is

$$\bar{\rho}_a \bar{L}_a \frac{d\bar{e}_a}{dt} = \frac{\bar{e}_u - \bar{e}_a}{\tau_u} + \frac{\bar{S}_a A_{sa} \bar{u}}{\tau_{ri} A_i}, \text{ and} \tag{26}$$

$$\bar{\rho}_b \bar{L}_b \frac{d\bar{e}_b}{dt} = \frac{\bar{e}_b - \bar{e}_i}{\tau_i} + \frac{\bar{S}_b A_{sb} \bar{u}}{\tau_{ri} A_i}. \tag{27}$$

Here, τ_u is analogous to equation (3), using $\dot{m}_u$ instead of $\dot{m}_i$. Finally, we describe species conservation for fuel and oxygen in the burned region. Again, we assume that the combustion reaction is quenched in the burned region. However, although the reaction is quenched, the species mass fractions can change because of changing boundary conditions at station i. Combining with mass conservation equations (22) through (24), the species equations are

$$\bar{\rho}_b \bar{L}_b \frac{dY_{fb}}{dt} = \frac{Y_{fb} - Y_{fi}}{\tau_i}, \text{ and} \tag{28}$$

$$\bar{\rho}_b \bar{L}_b \frac{dY_{ox,\,b}}{dt} = \frac{Y_{ox,\,b} - Y_{ox,\,i}}{\tau_i}. \tag{29}$$

Equations (22) through (29) describe the behavior of the inlet. A similar set of expressions applies to the tailpipe. A simple change of subscripts will produce the tailpipe equations.

Conditions at the ends of the inlet and tailpipe must be given careful consideration. Consider, for instance, the u end of the inlet pipe, which is open to ambient air. Both outflow and inflow will occur at this station. In the case of outflow, the pressure at this station is assumed to be equal to ambient pressure. For inflow, the flow properties at the pipe entrance are computed by assuming isentropic acceleration from the stagnant ambient conditions. A similar approach is used at stations i, e, and d.

2.4 Solution of the Governing Equations

We have developed conservation laws for each zone of the pulse combustor. Equations (2), (8), (10), (14) through (17), (20), and (21) describe the g and h regions in the combustion zone. Equations (22) through (29) apply to the inlet, with an analogous set for the tailpipe. These equations are solved by applying the Euler predictor-corrector algorithm. The solution method is straightforward and involves direct marching from one time to the next. Care should be used, however, at the junctions of the pipes with the combustor. Given the assumption of isentropic acceleration ***from*** the combustor ***into*** either pipe, velocity and pressure are related by a transcendental equation. Thus, we must iteratively root-find to produce boundary conditions that satisfy both the combustion zone and tailpipe zone equations. For flow ***into*** the combustor ***from*** either pipe, no iteration is needed because we assume that the fluid enters the combustor at the combustor pressure; i.e., a free-jet entrance. Similar comments apply to boundary conditions at stations u and d.

2.5 Mixing Model

Our equations can be solved numerically, but we must still describe the mixing rate between the g and h regions. The mixing process in this simulation is represented by the mixing time, defined by equation (11). This mixing time is essentially the reciprocal of the mixing rate, and depends on the details of the flow inside the combustor.

Bramlette [12] employed a model of diesel fuel injection and mixing [13] to describe the mixing process in a mechanically-valved pulse combustor. Bramlette quantified the mixing rate as the rate at which fresh charge was mixed with products to a specified ignition temperature, and calculated the mixing rate from the model of Rife and Heywood [13].

In the present analysis, we treat the mixing rate as a parameter, rather than defining it from a sub-model. However, sub-models, such as the one used by Bramlette, would form a logical extension of this work and could be easily incorporated into our equations. We used a relatively simple mixing model, employing step-change in the mixing rate. (Refer to Figure 3.)

This step-change approach is based on the work of Broadwell and Breidenthal [14] who describe mixing as a two-step process. The first step reduces large fluid eddies to small scale, with relatively slow mixing between species. The second step is a fast mixing process where small eddies are rapidly mixed by molecular diffusion. Figure 3 represents this two-step process in a pulse combustor. At time t_b, the contact surface enters the combustor, supplying fresh air to form the g-region. This fresh air mixes slowly while the initial eddy size is reduced. Fast mixing commences at time t_b and continues until the g-region is consumed at time t_c. Depending on the mixing rate and flow rate at station i, the g-region volume may disappear before the inlet flow reverses ($t_c < t_d$ as shown). Conversely, with different flow and mixing rates, some of the g-volume may continue to mix after the inlet flow reverses ($t_c > t_d$). We account for either possibility.

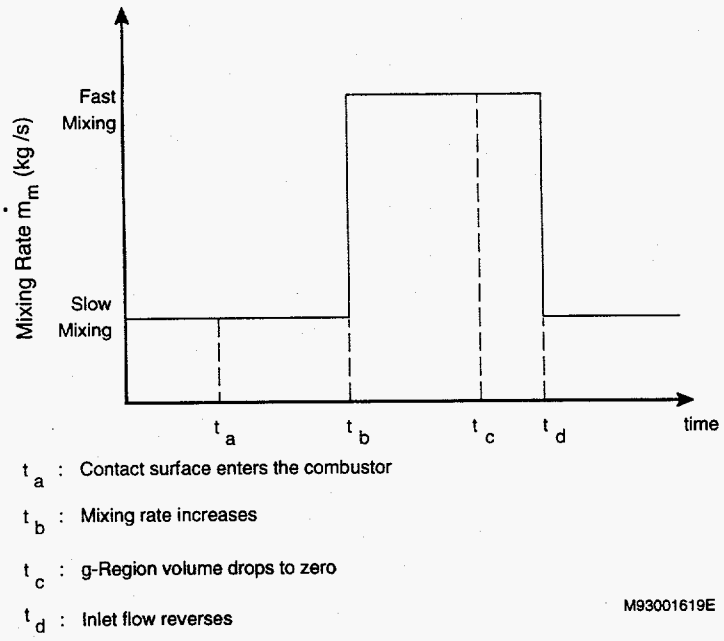

The model equations do not refer specifically to the mixing rate, but instead to the characteristic mixing time, τ_m, defined by equation (11). Thus, we define the following, which correspond to the mixing rates identified on Figure 3:

$\tau_{m,f}$ = the fast mixing time, corresponding to the fast mixing rate;

$\tau_{m,s}$ = the slow mixing time, corresponding to the slow mixing rate; and

t_Δ = the large eddy time, $t_b - t_a$.

Figure 3. The Two-step Mixing Process, Alternating Between the Fast and Slow Mixing Rates

2.6 Simulation Results - Effect of the Mixing Process

Table 1 lists those base-case parameters used in the simulation that we have neither discussed nor listed in the nomenclature. Pressure is specified upstream of the inlet.

Table 1. Model Base-Case Parameters

Parameter	Value
Pressure upstream of the inlet (status u on Figure 1)	106.9 kPa
Reference pressure	101.0 kPa
Reference temperature	300 K
Inlet length	0.102 m
Inlet diameter	0.0127 m
Tailpipe length	0.600 m
Tailpipe diameter	0.0191 m
Friction factor used for shear Stress calculation, eqs. (25)-(27)	0.03

This pressure forces air into the combustor, since this particular combustor is not self-aspirating. Geometric and operational parameters were selected to mimic the experimental configuration described in Section 3 of this report. We only varied the mixing parameters here, and we compare experimental data with fixed mixing parameters in Section 3.

Before describing the results, we remind you that equation (11) gives characteristic mixing times. These mixing times are not to be interpreted as the times required to mix the incoming air. Rather, they are the mixing times referenced to the fixed mass of gas that occupies the combustor at ambient conditions, equation (11). For example, a fast mixing time of 30 ms means that mixing is proceeding at a rate where one combustor volume of (ambient) gases would mix in 30 ms.

Thus, the intent of this discussion is to emphasize the sensitivity of calculated results to the mixing parameters. Figure 4 is a plot of the predicted pressure history for five different values of the mixing parameter, $\tau_{m,f}$. (The various plots are presented with a constant offset for better visibility; the scaled units are normalized pressure plus the offset.) All five cases have the same slow mixing time, $\tau_{m,s}$ = 100 ms, and eddy time, t_Δ = 0.01 ms. All five curves start from an initial transient high pressure that results from consumption of the initial fuel supply in the combustor. The lower curve represents the case where both the eddy time and the fast mixing time are small (0.01 ms). This corresponds to rapid mixing, which occurs as soon as the fresh charge enters the combustion zone. The initial transient decays after just a small oscillation, and then a steady flame results. (The flame is indicated by the temperature, which is not shown.) Progressing up through curves (B) through (E), $\tau_{m,f}$ increases to 50 ms. This progression corresponds to reduced mixing rates as the fresh charge immediately enters the combustor. The effect is a modest reduction in the amplitude of the initial transients following ignition as well as minor changes in the transient wave form. However, all cases result in a steady flame.

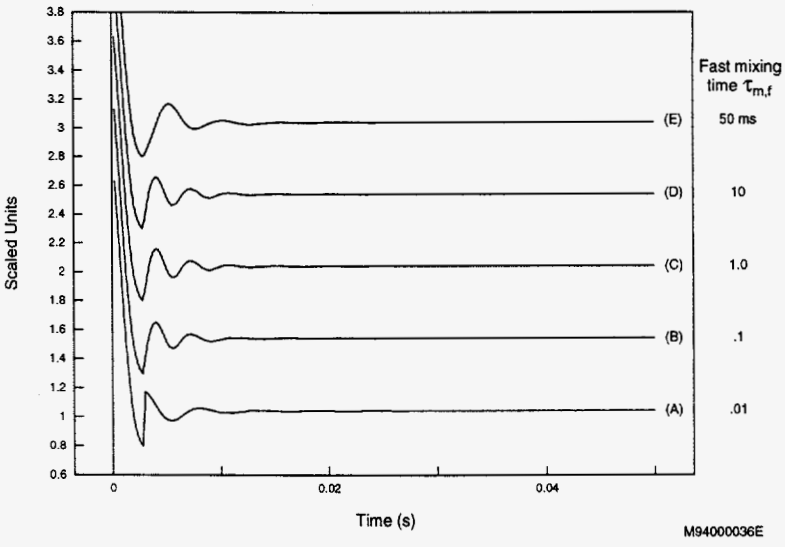

Figure 4. Effect of the Eddy Time, With τ_Δ = 0.01 ms

Figure 5 shows the effect of changes in the eddy time, t_Δ, but with fixed values, $\tau_{m,f}$ = 0.01 ms and $\tau_{m,s}$ = 100 ms. This effect corresponds to the rapid mixing that occurs

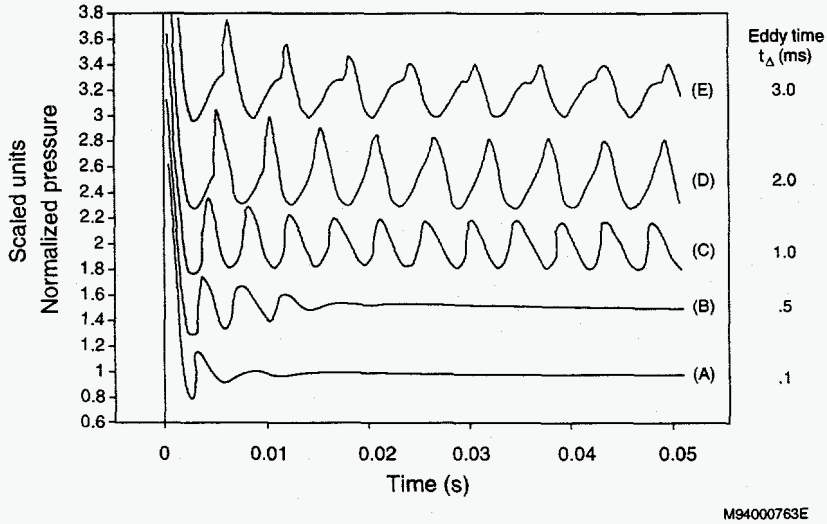

Figure 5. Effect of the Eddy Time, With $\tau_{m,f}$ = 0.01 ms

after some specified eddy time from the entry of the fresh charge into the combustor. Results are dramatically different from those shown in Figure 4 (note values of t_Δ). Initial transients are sustained longer in case (B), but are still replaced by a steady flame. As the eddy time is increased in cases (C) through (E), pulsations occur with varying amplitudes, frequencies, and wave forms. In each case, the nature of the pulsation can be rationalized by recognizing that a longer eddy time places the heat release later in the cycle.

Wood [15] noted that the relative timing of the heat release can have an effect on both the frequency and amplitude of pulsation. Frequencies in case (C) are higher than in case (D), because the heat release occurs before the natural acoustic pressure rise. In case (D), the heat release is more closely aligned with the resonant pressure, producing a lower frequency and higher amplitude. Finally, in case (E), the heat release is so late that a visible inflection point corresponds to the start of rapid mixing. The late heat release produces a lower frequency than in case (D), and again results in a lower amplitude because of the mismatch between heat release and acoustic resonance.

We show the results for cases (C), (D), and (E) in more detail in Figures 6, 7, and 8. The magnitude of each variable was scaled and offset to fit appropriately on the figures. The same scaling factor for each variable was used in all the figures so that the scaled units indicated on the y-axis can be used to compare magnitudes between cases. The zero for each variable was moved to make the graphs more readable. The variables are indicated to the right of each curve, with X representing the location of the inlet contact surface. This location X is measured from the upstream end of the inlet (station u in Figure 1); thus, the maximum value of X indicates that the contact surface has moved to the combustor inlet, station i.

Figure 6 corresponds to t_Δ = 1 ms, case (C) on Figure 5. Starting from the top graph, the contact surface is pushed out of the inlet during the high pressure part of the cycle, indicated by the minima on the X-curve. As the pressure drops (lower graph), the contact surface is drawn into the combustor, represented by the flat maxima on the X-curve. The g-volume immediately begins to grow. After 1 ms (i.e., the value of t_Δ), the fast mixing process begins, and the g-region volume is immediately reduced. The oxygen concentration rises abruptly, and the hot region temperature drops because cold air is mixed in. From this

point, the hot region temperature begins to rise, and oxygen is consumed as combustion proceeds. The relatively early fast mixing results in a fairly small g-volume, which produces a modest drop in T_h when fast mixing commences. The result is a rapid consumption of the oxygen as it is supplied from the g-region, followed by a slower reaction as additional oxygen mixes.

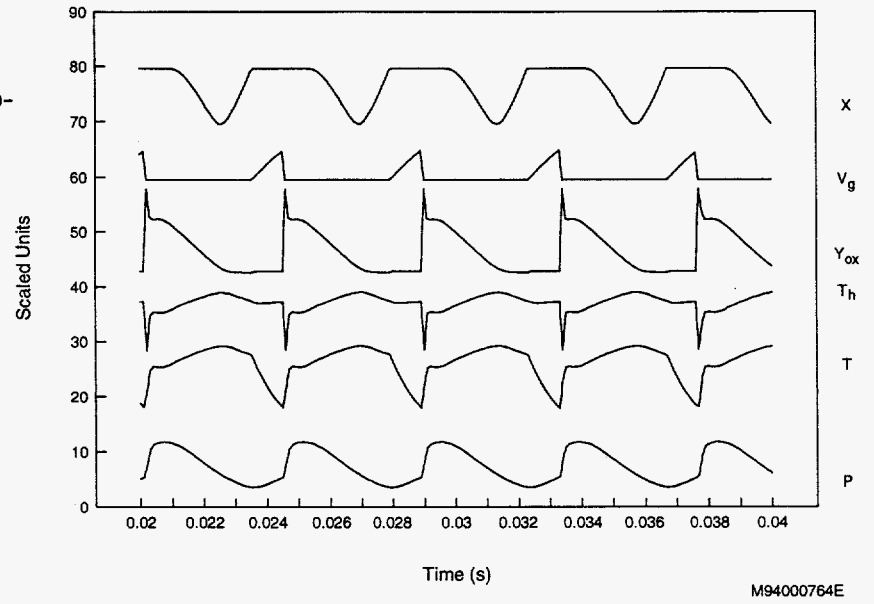

Figure 6. Time History of Various Parameters for Case (C) in Figure 5

Figure 7 corresponds to an eddy time of 2 ms, case (D) in Figure 5. The result is substantially different than that shown in Figure 6. A large drop in the hot region temperature occurs when the fresh charge commences fast mixing, with subsequent oxygen consumption reflecting combustion, which then raises the hot region temperature.

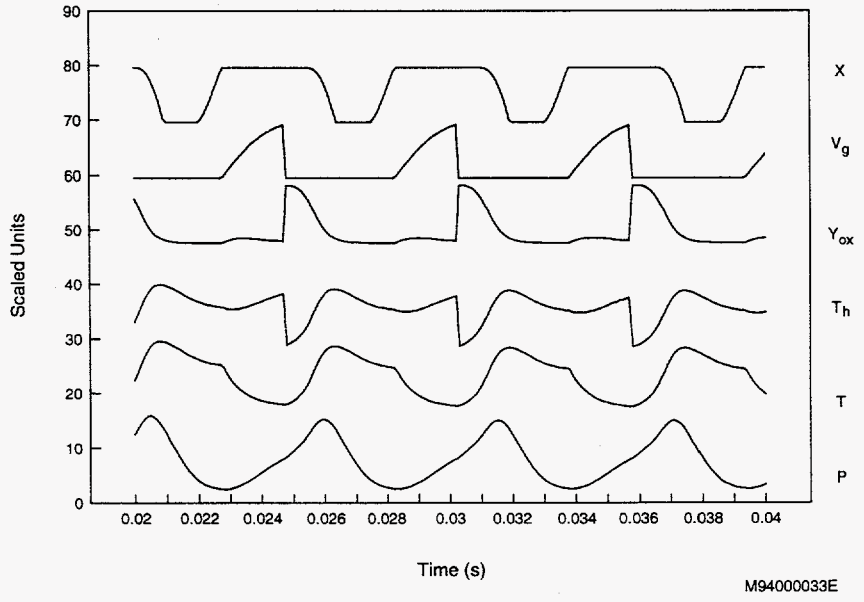

Figure 7. Time History of Various Parameters for Case (D) in Figure 5

Figures 6 and 7 show the effect of the eddy time when the fast mixing process occurs rapidly. In effect, fresh air is immediately mixed in the hot region after the eddy time. However, the mixing process probably occurs at a slower rate. Thus, Figure 8 shows the combined effect of limiting the fast mixing process to $\tau_{m,f}$ = 30 ms, and t_Δ = 2 ms, with other parameters being the same as those in Figures 6 and 7. Compared to the preceding cases, limiting the fast mixing process produces a significant change in the nature of the wave forms. The frequency and pressure amplitude in Figure 8 are lower than

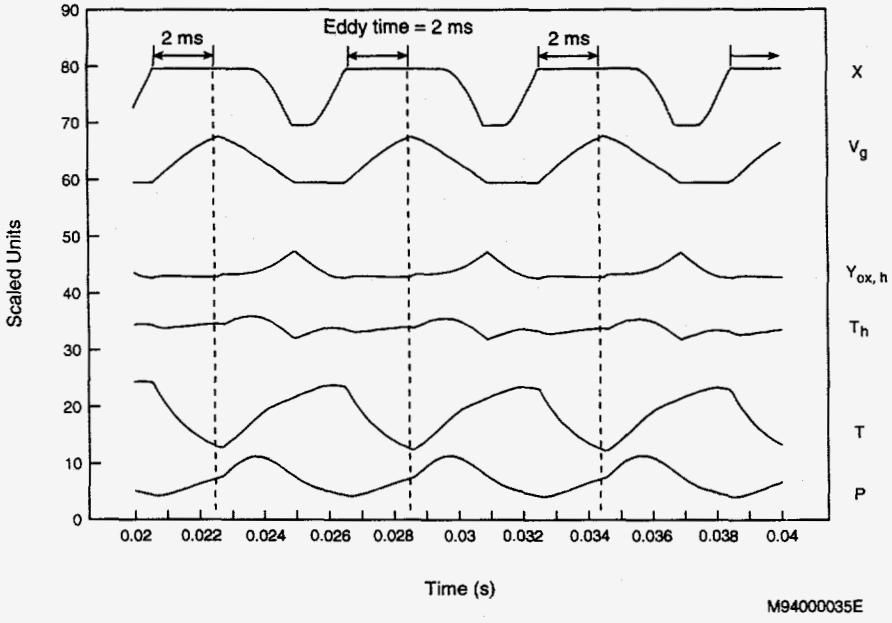

Figure 8. Time History for Various Parameters, With Mixing Time Scales $\tau_{m,s}$ = 100 ms, $\tau_{m,f}$ = 30 ms, and t_Δ = 2 ms

in Figure 7. Both are the result of spreading the heat release over a longer portion of the cycle. As might be expected, the amplitude of the ***average*** temperature, **T**, is the same in both cases. However, the amplitude of $\mathbf{T_h}$ differs remarkably between cases. Slowing the fast mixing process serves to flatten the hot-region temperature history, producing modest oscillations. The oxygen concentration in the hot-region is similarly affected. This result demonstrates the critical nature of the mixing process on both the pressure oscillation and the temperature-species history of gases moving through the system.

Although we have not focused on the temperature-species history of gases in the combustor, the model may be used to explain the effect of mixing on pollutant formation. For example, nitrogen oxides pollutants might be reduced by limiting the time span when high temperatures are associated with high concentrations of both oxygen and nitrogen. Figures 6 and 7 have such a temperature profile; high oxygen levels are associated with low values of $\mathbf{T_h}$, because the oxygen is mixed into the hot region faster than the reaction can consume it, quenching the hot region. However, in Figure 8, the hot region temperature, $\mathbf{T_h}$, is characterized by a smaller oscillation. Thus, oxygen is mixed into the hot region only slightly faster than the reaction consumes it, and a small surplus of oxygen persists at relatively high temperatures.

While the shape of these profiles cannot directly determine the final levels of pollutant produced, pollutant formation will clearly differ among combustors with various mixing processes. Keller and Hongo [16] showed that a reduced nitrogen oxides level in their experimental pulse combustor was the result of mixing cooler combustion products into the reacting mixture. These products were cooled by heat losses, not "quenched" by the incoming cold charge or returning tailpipe gases. The cold-charge quenching process occurs in Figures 6 and 7, while Keller and Hongo's scenario [16] is more consistent with the behavior in Figure 8. Thus, depending on the mixing process, different mechanisms may be involved in the formation of nitrogen oxides.

3 Experimental and Model Results

3.1 Experimental and Model Parameters

Figure 9 is a sketch of basic aerovalve pulse combustor geometry. The combustor has three distinct components: the inlet, the combustion chamber, and the tailpipe. Each of these components is defined by a length and diameter as shown. An inlet plenum is defined by the lines enclosing the inlet; air supplied to the inlet plenum passes through the pulse combustor from left to right. The pressures $\mathbf{P_{1o}}$, $\mathbf{P_{2o}}$, and $\mathbf{P_{3o}}$ are the ***mean*** stagnation pressure values for the inlet plenum, the combustion chamber, and in the jet exiting the tailpipe.

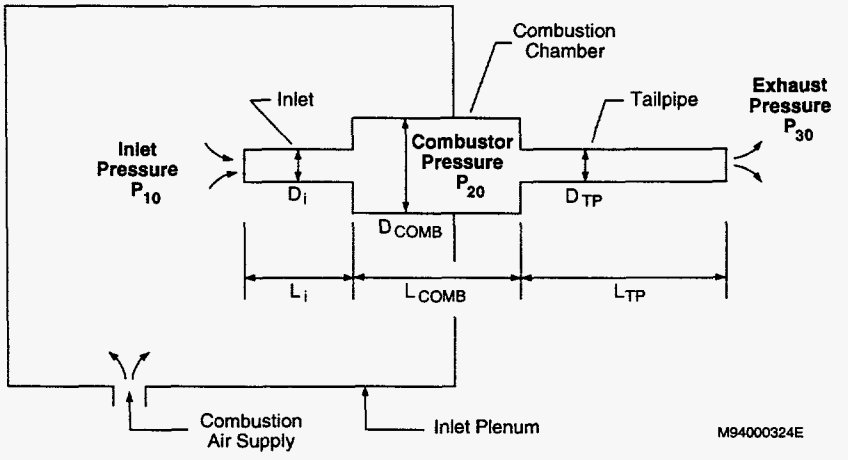

Figure 9. Schematic of an Aerovalve Pulse Combustor

We present various mean pressure differences through the pulse combustor, because these pressure differences are an indicator of pressure gain performance. The pressure gain process effectively pumps air through the combustor, raising the stagnation pressure of gases passing through the system, such that $\mathbf{P_{1o}} < \mathbf{P_{2o}}$. The stagnation pressure $\mathbf{P_{2o}}$ will be converted to kinetic energy in the tailpipe; if losses are small $\mathbf{P_{3o}}$ will also be greater than $\mathbf{P_{1o}}$. This is in contrast to a conventional steady combustor, where it would follow that $\mathbf{P_{1o}} > \mathbf{P_{3o}}$, since the combustion air must overcome various losses to pass through the system.

While the pressure gain process will indeed occur with correct timing of the various unsteady flows [6], there is little guidance on how to design a combustor that will produce pressure gain. The various lengths and diameters shown in Figure 9 present a wide range of possible geometric combinations that may affect combustor performance. The model presented in Section 2 of this report was developed specifically to allow rapid investigation of these geometric parameters.

In this section, we compare laboratory data to model predictions to prove that the model does indeed capture the basic features of combustor performance, and we use the model to explain aspects of the laboratory data.

Except as noted, the numeric simulation in Section 2 was performed with a fixed set of three parameters $\tau_{m,s}$, $\tau_{m,f}$, and t_Δ:

$$\tau_{m,s} = 100 \text{ ms}, \ \tau_{m,f} = 30 \text{ ms, and } t_\Delta = 2 \text{ ms}. \tag{30}$$

This particular set of parameters was chosen after identifying that the largest effect on oscillation came from the eddy time. Several values of the eddy time were tested; the chosen value of 2 ms provides reasonable agreement with most of the data.

3.2 Experimental Description

The experimental pulse combustor is shown in Figure 10. The pulse combustor is fashioned from standard straight-walled pipe components, mounted inside a 20-cm diameter sheet-metal duct. The duct is divided into three plenums, which are (left to right) the inlet plenum, the dilution plenum, and the exhaust plenum. Combustion air enters the inlet plenum, passes through the pulse combustor inlet, reacts with fuel in the combustion chamber of the pulse combustor and passes into the exhaust plenum. (Note that the inlet pipe is not shown attached in the upper figure to clearly show the fuel entry point.) The dilution plenum is not directly relevant to this investigation; dilution air is added merely to lower the temperature of the exhaust before it exits the laboratory. The concentric baffles at the right end of the dilution plenum serve to provide an axi-symmetric, dilution, mixing region that is downstream of the pulse combustor tailpipe. This mixing region is the subject of a separate study [17].

The lower portion of Figure 10 is a detailed cross-section of the pulse combustor. Natural gas fuel entered the combustor through a 3.1-mm tube that was cantilevered along the axis of the pulse combustor. The commercial-grade natural gas had a composition of approximately 91 percent methane, 6 percent ethane, and 2 percent higher hydrocarbons and inerts. (During actual testing, this composition was monitored and showed negligible variation over the course of the testing.)

Fuel entered the combustor through two 1.5-mm holes at the tip of the injection tube. The combustor was manufactured from standard pipe unions that were welded together to allow different size inlets to be readily attached. Figure 10 shows that a spark plug was used for ignition and that a 6.4-mm tube extended through the exterior duct where a tee-connection measured mean pressure and dynamic pressure in the combustion chamber. For the flow rates studied, the mean velocity in the combustion chamber was small enough that the combustion chamber's mean static and stagnation pressures were treated as approximately equal. The mean pressure was measured with a water manometer, preceded by a 7-m long coil of tubing. The tubing served to damp oscillations, which would otherwise arrive at the water manometer.

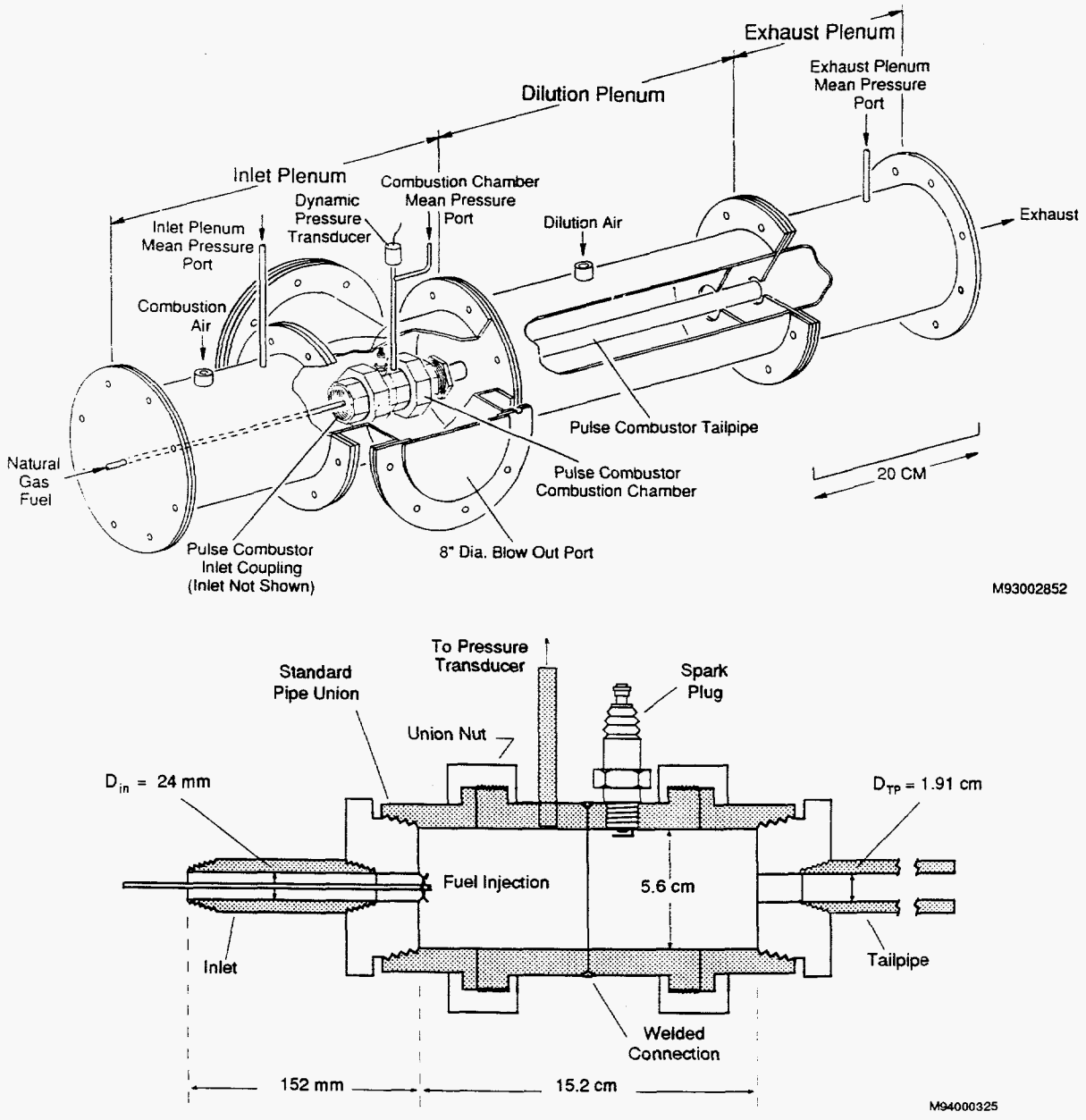

Figure 10. Experimental Pulse Combustor

Tests without the tee-connection and with transducer connection tubes of various lengths were conducted to ensure that the dynamic pressure signal was not influenced by acoustics in the connecting tube. The dynamic signal was essentially unchanged by these various modifications, except when the tubing length matched a resonant wavelength, which was avoided in all tests. The dynamic pressure was measured with a piezoelectric transducer, and the amplified output was digitized and stored on a personal computer for subsequent analysis.

The mean pressure of the inlet plenum was monitored with a diaphragm-type, electronic, differential-pressure gauge that was connected through a port attached to the top of the plenum. Initial tests using a dynamic pressure transducer in this location showed that the inlet plenum experienced a small amplitude pressure oscillation during operation. However,

the amplitude was typically less than 1 percent of the combustion chamber oscillation; this was considered negligible. The mean pressures of the inlet plenum and combustion chamber were measured as a differential pressure compared to the mean pressure of the exhaust plenum. This provided a measure of pressure drop across the various components while accounting for any backpressure in the exhaust system. Figure 10 does not show that the exhaust plenum extended more than 6 m before exiting the laboratory building. A muffler was used at the end of the exhaust plenum, which introduced a small amount of backpressure (less than 0.25 kPa).

3.3 Comparison of Experimental and Numeric Results

The combustor geometry shown in Figure 10 was treated as a baseline case. With a combustion air flow ranging between 2 and 8 g/s, this geometry produced oscillating combustion in a frequency range of 150 to 190 Hz, depending on operating conditions. A typical oscillating pressure signal is shown in Figure 11. Wave forms were generally pure sinusoids. However, as shown later, inadequate mixing rates at low air flows can lead to irregular oscillations.

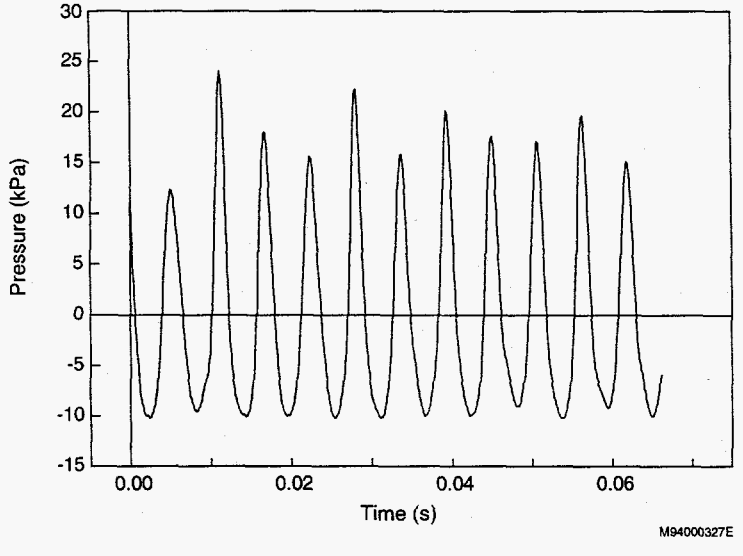

Figure 11. Typical Pulse Combustor Pressure Signal

Geometric parameters match the experimental dimensions shown in Table 2, using the nomenclature shown in Figure 9. The numeric model was run interactively, with the user specifying an upstream pressure and temperature equal to the measured laboratory values. The simulation generally overpredicted the air mass flow rate at a given plenum pressure. In addition, the simulation seldom predicted stable oscillations for fuel-lean conditions. The failure of the model to predict fuel-lean operation is similar to the result reported by Richards et al. [8]

Table 2. Dimensions of the Base-Case Combustor

Lengths (m)			Diameters (m)		
Inlet	L_i	0.102	Inlet	D_i	0.0127
Tailpipe	L_{tp}	0.600	Tailpipe	D_{tp}	0.0191
Combustor	L_{comb}	0.152	Combustor	D_{comb}	0.0556

in their thermal pulse-combustor model. The observed discrepancy for the fuel-lean cases may be the consequence of the simplified kinetic scheme used by Kretschmer and Odgers [10]. Stated another way, the model predicts that stable oscillations occur at higher fuel flow rates than those actually observed in the lab. Because the model will seldom predict stable oscillations for fuel-lean operation, all numeric results are reported at a fixed equivalence ratio of 1.05. However, because of material limitations, the laboratory data was collected at an equivalence ratio of 0.82.

Figure 12 compares laboratory data and measurements from the laboratory combustor. The frequency is predicted reasonably well (Figure 12a), except at the lower flow rates, where the mixing process in the experiment is probably slower than that suggested by the set of mixing parameters chosen in equation (30). In Figure 12b, the measured and predicted root-mean-square pressure levels agree well over the operation range. In Figure 12c, measured and predicted pressure differences between the inlet and the combustion chamber are in reasonable agreement, especially in regard to trend. Notice that this quantity is a measure of pressure loss. If the combustor were producing pressure gain, this measured pressure difference would be negative. Results presented later will demonstrate how geometric changes can achieve the desired pressure gain result.

The model results in Figure 12 were established with constant mixing parameters. While a brief study of mixing parameters (in Section 2) allowed selection of mixing parameters that match higher flow-rate data, equation (30), the greatest discrepancy between experimental and model results occurs at low flow rates, where the mixing process has little kinetic energy to stir the reacting mixture.

Figure 13 thus compares the laboratory pressure oscillation to the model prediction for several different mixing parameters. The bottom curve (A) is the laboratory signal that corresponds to the lowest flow rate shown in Figure 12. At this low flow rate, the laboratory combustor pressure signal was somewhat erratic, with some "beating" character. Curve (B) is the model pressure signal, with the mixing parameters identified in equation (30). The frequency is clearly over-predicted, and the model predicts a stable oscillation. In curve (C), the mixing times $\tau_{m,f}$ and $\tau_{m,s}$ are doubled, and the frequency is reduced. Still, the model predicts a periodic oscillation. However, in curve (D), the eddy time is increased to 2.5 ms, and now the beating phenomenon is clearly predicted.

The period of oscillation within the beating envelope is still less than that observed on the laboratory curve (A), and the period of the beating envelope itself is comparable to the observed laboratory data. In curve (E), the eddy time is set again to 2 ms, but the mixing times are increased once more by a factor of 1.5. The result is an irregular oscillation, showing neither beating nor a recognizable pattern. If the eddy time is again increased to 2.5 ms, curve (F) shows that the irregular oscillation in curve (E) is again replaced by a periodic cycle.

While the laboratory pressure oscillation is not exactly predicted, the numeric model predicts a wide range of possible behaviors, depending on the mixing process. Most interesting, curve (E) appears to exhibit an irregular oscillation, even though all input processes are well-defined in the numeric model. One may speculate that the irregular

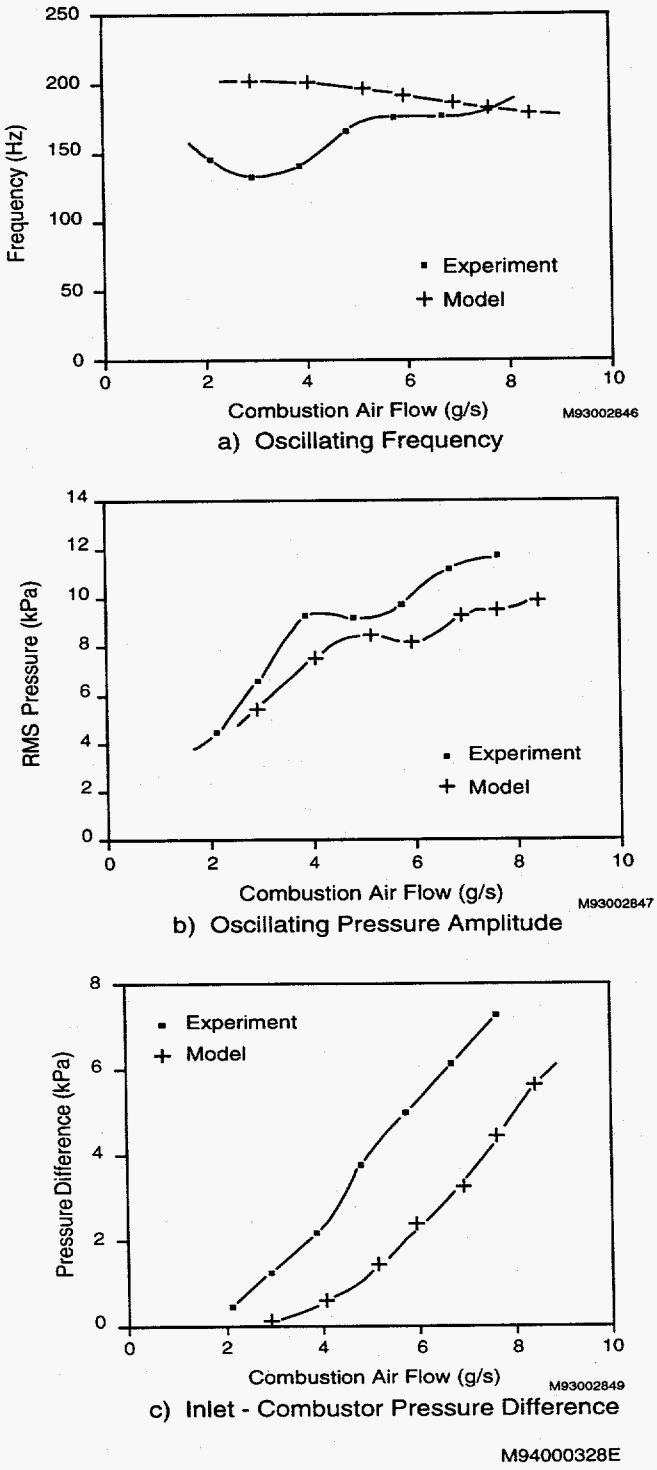

Figure 12. Comparison of Laboratory Data and Model Predictions for Frequency, Oscillating Pressure Amplitude, and Pressure Differences

oscillations observed in the lab (curve A) are not solely the result of random variations in the mixing process, but are a natural consequence of the non-linear processes involved. Indeed, it has been shown both theoretically and experimentally that other kinds of pulse combustors will oscillate in a chaotic fashion [18, 19], even with well-defined input parameters.

3.4 Effect of Combustor Geometry

We developed our model to help identify the effect of changes to combustor geometry. Figures 14 and 15 compare model and experimental results as a function of combustor inlet length. We ran the model by iteratively selecting an inlet pressure to produce the same flow rate as existed in the lab (6 g/s). Again, the lab data was limited to an equivalence ratio of 0.82, but the simulation was performed at a ratio of 1.05. As before, the mixing process was fixed for these comparisons, with the same parameters from equation (30).

Both laboratory data and model predictions demonstrate that inlet length has a

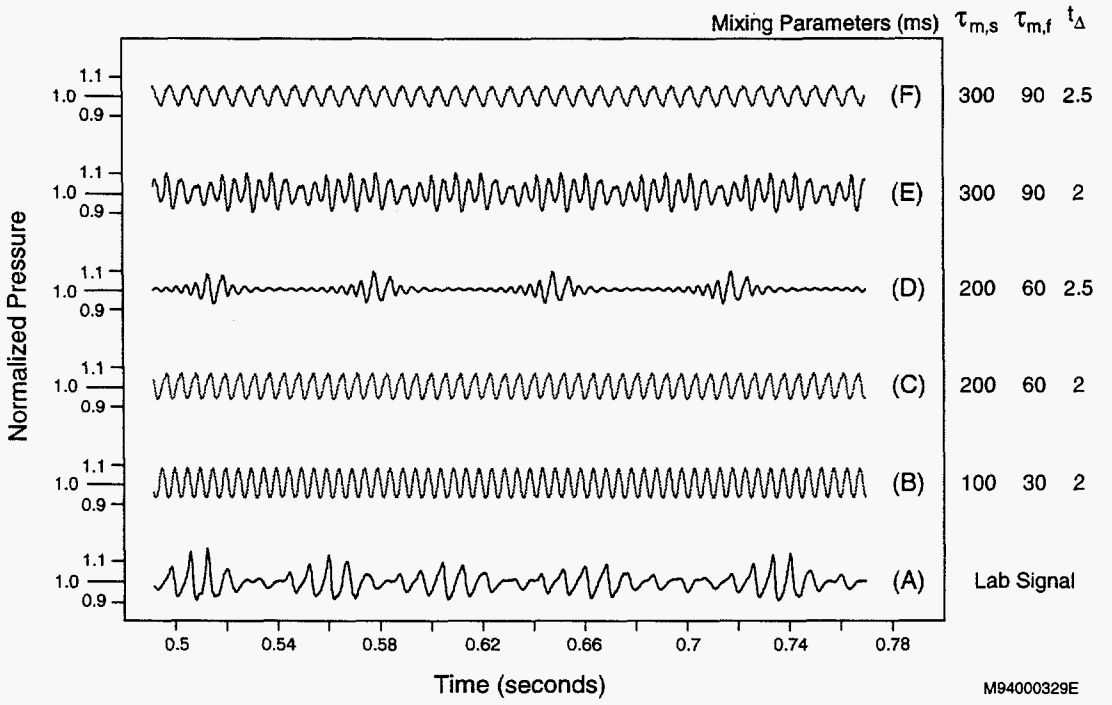

Figure 13. Comparison of the Laboratory Pressure Signal (A) to Model Predictions for Several Different Values of the Mixing Parameters (B) - (F)

marked effect on combustor performance. Understandably, the operating frequency is reduced. At lower frequencies, the root mean square (RMS) pressure is expected to be larger since comparable flow rates require more heat release per cycle; this is evident in both laboratory and numeric results. Figures 15a and 15b compare pressure differences for numeric and experimental results. The numeric simulation over-predicts pressure differences in most cases. However, the qualitative behavior of the various pressure differences is similar in both the simulation and the

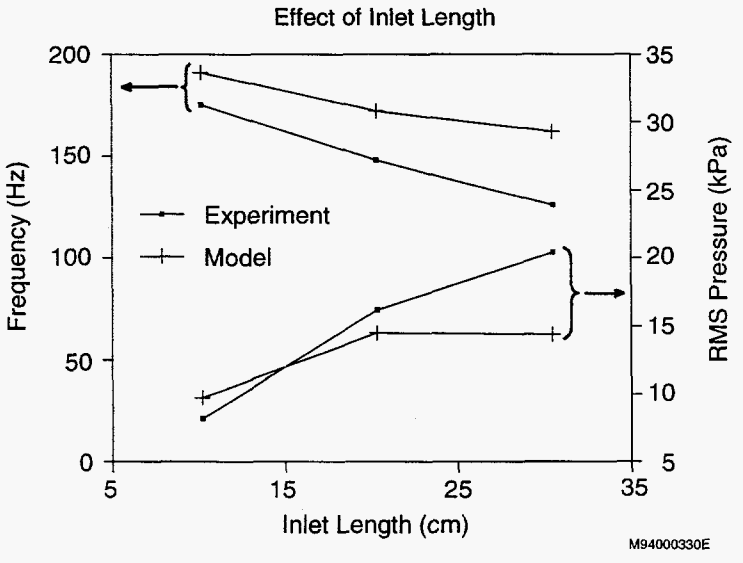

Figure 14. Laboratory Data and Model Predictions for Frequency and RMS Pressure as a Function of Inlet Length

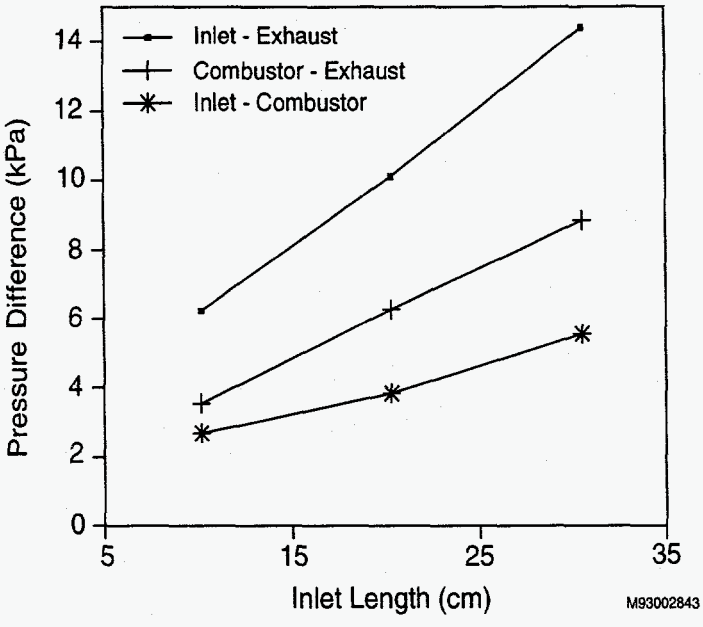

a) Effect of Inlet Length: Numeric Model

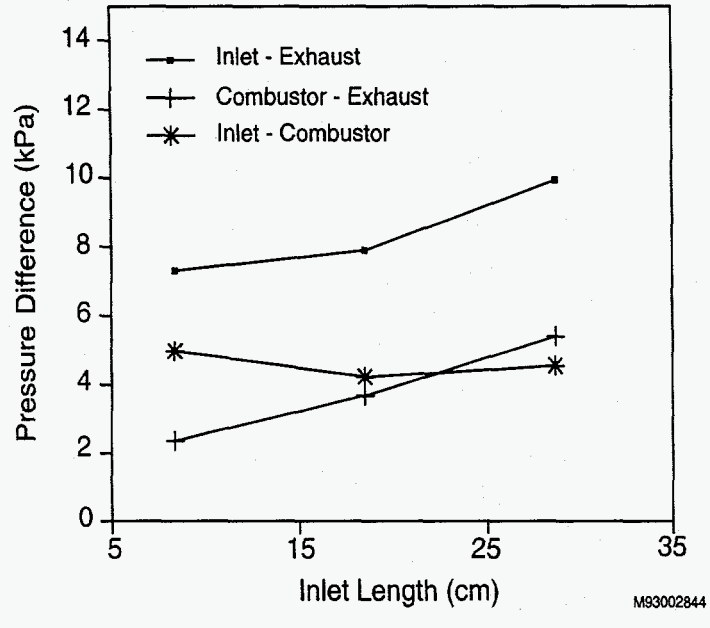

b) Effect of Inlet Length: Experimental Results

Figure 15. Model Predictions (a) and Laboratory Data (b) for Pressure Difference as a Function of Inlet Length

laboratory data, with some difference for the inlet-combustor pressure difference.

The laboratory data show that the inlet-combustor pressure difference is nearly insensitive to inlet length, whereas the numeric model shows a modest increase in pressure difference with increased inlet length. However, it was initially surprising that both experimental and numeric results show ***tailpipe pressure drop*** being approximately doubled by increasing ***inlet length*** from 10 to 30 cm. This was unexpected because all the cases shown in Figure 15 have the same mean flow properties, including mass flow. Thus, the longer ***inlet*** case needs twice the mean pressure to drive the same mass flow through the ***tailpipe***.

This result is attributed to the ***unsteady*** nature of the flow. This is shown by inspecting the tailpipe velocity predicted by the model, Figure 16. The higher amplitude, low frequency oscillation associated with the longer inlet causes significant flow reversal (i.e., negative velocities) in the tailpipe. The shorter inlet, with a higher frequency and lower amplitude oscillation, shows little tailpipe flow reversal. The net effect of the flow reversal is that the tailpipe is effectively "blocked" to exiting gases for a portion of the combustor cycle. This blockage results in a higher mean pressure to drive out the same quantity of gas through the tailpipe, consistent with Figure 15.

3.5 Geometric Configurations for Pressure Gain

The behavior we have described emphasizes the complex interaction among various combustor components. If one wishes to optimize a combustor design for pressure gain, it is inadequate to consider the effect of changes to a single geometric parameter. Changes to the inlet may produce unexpected results because of interaction with a specific tailpipe geometry.

However, the model's pressure gain predictions can be validated against results presented by Kentfield [6], who developed a specific combustor geometry capable of producing pressure gain [7]. A direct simulation of the Kentfield geometry (excluding a taper on the tailpipe) predicted very strong pressure gain, as long as the mixing process was fast enough. Rather than directly repeat the Kentfield geometry for laboratory tests, we noted that the existing combustor volume (Table 2) was smaller than the Kentfield geometry by a factor of 1.7.

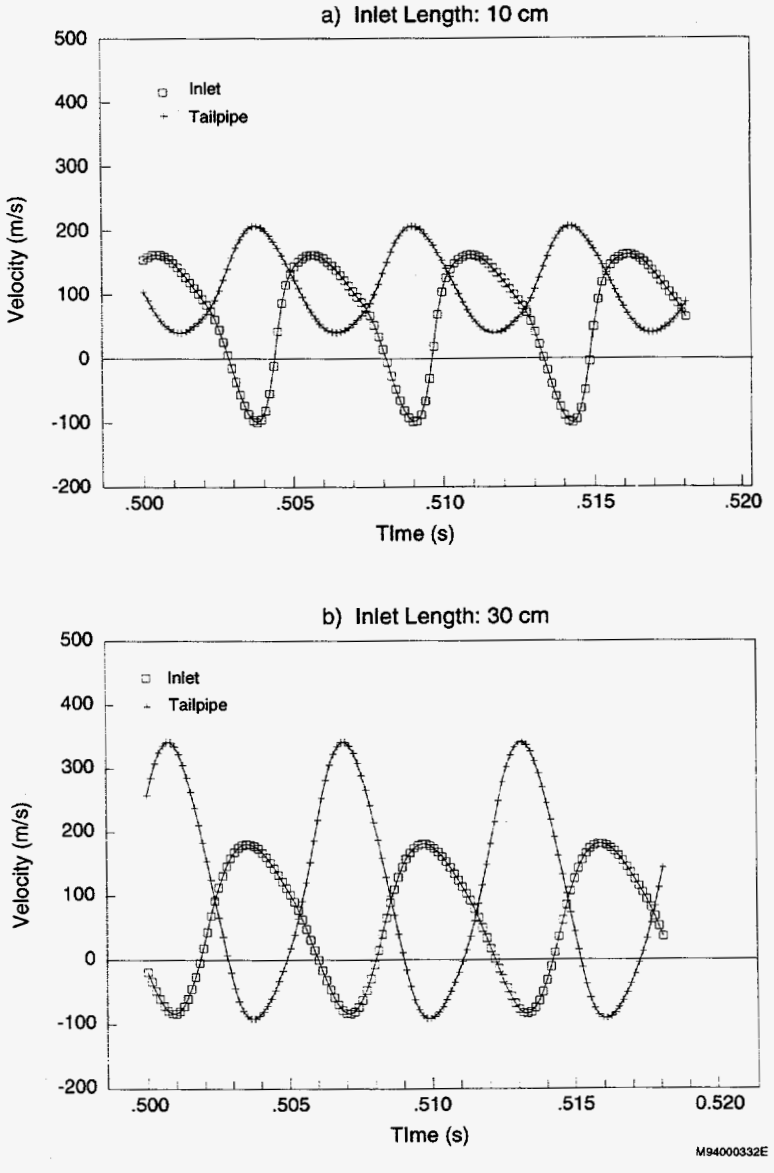

Figure 16. Model Predictions of Inlet and Tailpipe Gas Velocities for Inlet Lengths of 10 and 30 cm

In principle, the model equations presented in Section 2 of this report suggest a method for scaling the rest of the pulse combustor dimensions to match this reduced volume. Careful inspection of the governing equations will show that except as noted below, the combustor volume does not appear directly. Other than the exceptions, the volume is divided by the inlet (or tailpipe) cross-section, for the characteristic lengths $\mathbf{L_{ri}}$ (and an associated tailpipe characteristic length, $\mathbf{L_{r,tp}}$). This can be verified in equation (3), for example, by writing the mass flow $\dot{m}_i$ as the product of the inlet density, velocity, and inlet area, $\mathbf{A_i}$; the characteristic length $\mathbf{L_{ri}}$ will result. Thus, except as noted below, a given combustor could be scaled to a different volume simply by holding $\mathbf{L_{ri}}$ and $\mathbf{L_{r,tp}}$ constant. Notice that the inlet

(and tailpipe) lengths are normalized with L_{ri} (and $L_{r,tp}$) so that the physical lengths of both inlet and tailpipe are unchanged when scaling.

Exceptions to this scaling approach occur in three processes: mixing, frictional flow losses, and heat transfer. Referring to heat transfer time, equation (7) and mixing time, equation (11), combustor volume is not normalized by the inlet area. Changes to the combustor volume will alter these terms. Likewise, frictional losses in the inlet (and tailpipe) are accounted for by the cross-section-to-surface-area ratios in equations (25) through (27), and these will change with changes to the inlet or tailpipe cross sections. However, estimates of the contribution of these various terms were relatively small when considering scaling from the Kentfield geometry. Consequently, it was possible to scale the Kentfield geometry by merely holding the ratio of the combustor volume to inlet area as a constant.

The resulting geometric parameters are shown in Table 3. The combustion chamber dimensions are the same as those shown in Table 2; this particular geometry was readily installed in the lab by changing the inlet and tailpipe geometry from the base-case geometry.

Table 3. Dimensions of the Pressure-Gain Combustor

Lengths (m)			Diameters (m)		
Inlet	L_i	0.152	Inlet	D_i	0.0222
Tailpipe	L_{tp}	0.900	Tailpipe	D_{tp}	0.0191
Combustor	L_{comb}	0.152	Combustor	D_{comb}	0.0556

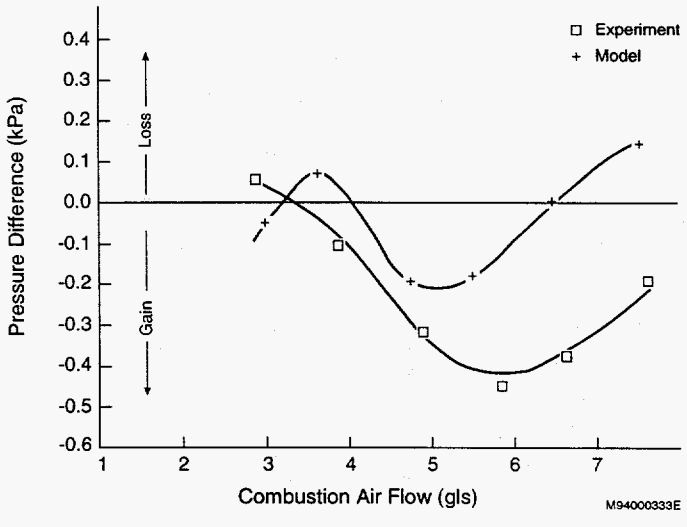

Figure 17. Inlet-Combustor Pressure Difference for the Scaled Combustor Geometry Listed in Table 3

Figure 17 compares measured and predicted pressure differences of the inlet-combustion chamber for the geometry listed in Table 3. Mixing parameters were the same as in earlier cases, and again, the simulation was performed at an equivalence ratio of 1.05 while lab tests were limited to a 0.82 equivalence ratio. Pressure gain is indicated by a negative pressure difference.

The pressure-gain magnitude differs for predicted versus measured cases, but the minimum in the laboratory data and numeric predictions suggests that an optimum flow rate exists for pressure gain, as may be expected. For a given combustor

geometry, the "pumping" action of the pressure gain combustor can ideally process a specific quantity of air. Supplying more or less air simply reduces the effectiveness of the process, much like limiting or supplying excess air to a mechanical air compressor (with a fixed outlet pressure) will reduce the compressor effectiveness.

The numeric results shown in Figure 17 were fairly sensitive to geometric and operational parameters. The predicted pressure difference curve could be substantially shifted with relatively modest changes in various parameters, including geometric parameters. We are presently investigating these effects.

4 Summary and Conclusions

We have presented a control-volume formulation for the conservation laws that describe an aerovalve pulse combustor. We used a single-step bi-molecular reaction to describe combustion, and we prescribed the mixing process between fresh air and combustion as a two-step process, with fuel and air initially mixing slowly. After a specified delay time, the mixing rate is increased. In the cases we studied, delay time had a significant effect on combustor behavior. Small delay-time values produced steady combustion, while progressively larger values produced wave forms of varying amplitude and frequency.

The model is relatively simple; the governing equations were solved on a VAX 6520 computer and run interactively. The calculation and output to the screen occurred at approximately 1/20 of the real time; i.e., a simulation of a 100-Hz oscillation was computed at a 5-Hz rate. While the computational speed provides an opportunity to explore the effects of many geometric and operating parameters, the model equations are themselves useful because they identify all the characteristic length and time scales relevant to the design of an aerovalve pulse combustor. For example, careful inspection of the equations reveals that the inlet diameter does not directly appear anywhere in the governing equations, but is embedded in the characteristic length, $\mathbf{L_{r,i}}$, which is the ratio of combustor volume to inlet area. Except as noted, a given pulse combustor may be scaled in size by simply holding $\mathbf{L_{r,i}}$ constant, along with other parameters identified in the equations. Exceptions to this scaling approach occur in the mixing process, the heat transfer, and fluid friction losses.

Use of this model to explore rapid geometric and operational changes in a pulse combustor is subject to the assumed mixing parameters, and also to validation that the simple control volume formulation can correctly capture the operating physics. We have demonstrated that changes to the mixing rate affect the temperature-species history of gases in the combustor. This behavior may have significant influence on the production of pollutants, such as nitrogen oxides.

In Section 3 of this report, we compared experimental measurements from an aerovalve pulse combustor to predictions from the model described in Section 2 of this report. We found that the model can assess the effects combustor geometry, operational parameters, and mixing processes have on pulse combustor performance. We show that laboratory data and model predictions were generally in good agreement for fixed mixing parameters, except at low combustion air flow rates. Model results suggest that poor mixing may cause the irregular oscillations observed in the lab at low air flow rates. Either numerically or experimentally increasing the combustor inlet length produced an unexpected increase in the tailpipe pressure difference. This result was attributed to flow reversal produced in the tailpipe when using a longer inlet. We were able to scale a published combustor geometry to produce pressure gain using the scaling relations present in the model. This approach was verified both experimentally and theoretically.

Because the model presented in Section 2 is computationally very simple, it is possible to survey a wide range of geometric and operating conditions to find the desired pressure gain performance. In fact, we are conducting a numeric survey of combustor geometries that

covers thousands of geometric and operating combinations. Promising cases will be investigated in the laboratory, at 1 atm and at elevated pressures [20].

No prior work seems to have been aimed at optimizing combustor geometry for high-pressure operation, and the present approach of combining numeric predictions with laboratory data should expedite the development of a pressure-gain combustor that is suitable for gas turbine applications.

5 Nomenclature

A	cross-sectional area
A_s	surface area
C_p	constant pressure specific heat, 1350 J/kg/K.
e	internal energy per unit mass
F	unit step function defined by equation (9)
G	unit step function, defined by equation (19)
h	heat transfer coefficient for the combustion zone walls, 120 $W/m^2/K$.
K	kinetic coefficient, equation (18), 1.576×10^9 s^{-1}
L_a	length of the "unburned" region of inlet
L_b	length of the "burned" region of inlet
L_i	total inlet length; $L_i = L_a + L_b$
L_{ri}	reference inlet length; $L_{ri} = V_c/A_i$
$\dot{m}$	mass flux
P	pressure in the combustion chamber
$\dot{Q}$	heat release per unit volume
R	specific ideal gas constant, $287 \frac{J}{kg} K$
S	shear stress at the inlet (or exit) pipe wall calculated from Schlichting [11] pipe formula, normalized by the ambient pressure
S_R	the stoichiometric ratio for the mass of oxygen consumed per mass of fuel burned
T	temperature

$\bar{T}_{act}$	The dimensionless activation temperature, equation (18), 50
T_w	combustion zone wall temperature, 1200 K
u	velocity
u_r	reference velocity; $\sqrt{RT_a}$
V	volume
γ	ratio of specific heats, 1.27
τ_c	combustion time, equation (6)
τ_e	exit flow time, equation (5)
τ_f	fuel flow time, equation (4)
τ_{HT}	heat transfer time, equation (7)
τ_i	inlet flow time, equation (3)
τ_m	mixing time, equation (11)
τ_{ri}	reference inlet time; $\tau_{ri} = L_{ri}/\sqrt{RT_A}$
τ_u	flow time associated with station u, analogous to equation (3) using $\dot{m}_u$
ΔH_f	fuel heat of combustion per unit mass $4.6 \times 10^7 \frac{J}{kg}$

Subscripts

A	designates ambient properties
a	designates "unburned" region of inlet
b	designates "burned" region of tailpipe
c	corresponds to combustion region
d	conditions at station d (Figure 1)

e	conditions at station e (Figure 1)
f	corresponds to fuel
g	designates cold region of combustion zone
h	designates hot region of combustion zone
i	conditions at station i (Figure 1)
o	stagnation property
ox	corresponds to oxygen
u	conditions at station u (Figure 1)

6 References

1. Adams, C.W., Performance Results of the Lennox Pulse-Combustion Furnace Field Trials, *Proceedings of the Symposium on Pulse Combustion Applications*, Vol. 1, Atlanta, GA, March 2-3, 1982, Gas Research Institute, Report GRI-82/0009.2, 1982.

2. *Gas Research Institute Digest*, pp. 32-33, Fall/Winter 1991.

3. Pulse Combustion Sounds Off, *Chemical Engineering*, 28-35, November 1990.

4. Keller, J.O., Bramlette, T.T., Barr, P.K., and Alvarez, J.R., No_x and CO Emissions from a Pulse Combustor Operating in a Lean Premixed Model, *The 25th (International) Symposium on Combustion*, July 31 - August 5, Irvine, CA, 1994.

5. Kentfield, J.A.C., Rehman, A., and Cronje, J., Performance of Pressure-Gain Combustors Without Moving Parts, *Journal of Energy*, Vol. 4, No. 2, pp. 56-63, 1980.

6. Kentfield, J.A.C., and Fernandes, L.C.V., Improvements to the Performance of a Prototype Pulse, Pressure-Gain, Gas Turbine Combustor, *Journal of Engineering for Gas Turbines and Power*, Vol. 112, pp. 67-72, 1990.

7. Olorunmaiye, J.A., Numerical Simulation and Experimental Studies of Highly Loaded Valveless Pulsed Combustors, Ph.D. Thesis, Univ. of Calgary, Calgary, Alberta, 1985.

8. Richards, G.A., Morris, G.J., Shaw, D.W., Keeley, S.A., and Welter, M.J., Thermal Pulse Combustion, *Combustion Science and Technology*, Vol. 94, pp. 57-85, 1993.

9. Moody, F.J., *Introduction to Unsteady Thermofluid Mechanics*, John Wiley & Sons Publishing, 1990.

10. Kretschmer, D., and Odgers, J., Modelling of Gas Turbine Combustors - A Convenient Reaction Rate Equation, *Journal of Engineering for Power*, pp. 173-180, July 1972.

11. Schlichting, H., *Boundary-Layer Theory*, McGraw-Hill Publishers, Seventh Edition, p. 597, 1979.

12. Bramlette, T.T., *The Role of Fluid Dynamic Mixing in Pulse Combustors*, Sandia National Laboratory, SAND87-8622, 1987.

13. Rife, J., and Heywood, J.B., Photographic and Performance Studies of Diesel Combustion With a Rapid Compression Machine, *SAE Transactions*, Vol. 83, pp. 2942-2961, 1974.

14. Broadwell, J.E., and Breidenthal, R.E., A Simple Model of Mixing and Chemical Reaction in a Turbulent Shear Layer, *Journal of Fluid Mechanics*, Vol. 125, pp. 397-410, 1982.

15. Wood, A., *Acoustics*, Dover Publications, pp. 92-93, 1966.

16. Keller, J.O, and Hongo, I., Pulse Combustion: The Mechanisms of NOx Production, *Combustion and Flame*, Vol. 80, pp. 219-237, 1990.

17. Gemmen, R.S., Rogers, W.A., and Richards, G.A., Experimental and Numerical Investigation of a Confined Pulse Combustor Tailpipe Exhaust Mixing with a Steady Jet, *Central and Eastern States Section Joint Meeting of the Combustion Institute*, New Orleans, LA, March 15-17, 1993.

18. Daw C.S., Richards, G.A., and Thomas, J.F., Modelling Deterministic Chaos in Thermally-Pulsed Combustion, *The Combustion Institute*, Central States Meeting, Columbus, Ohio, April 26-28, 1992.

19. Narayanswami, L., Daw, C.S., Thomas, J.F., and Richards, G.A., Deterministic Chaos in Thermal Pulse Combustion, in review, *Chaos*, 1994.

20. Gemmen, R.S., Richards, G.A., and Janus, M.C., Development of a Pressure-Gain Combustor for Improved Cycle Efficiency, ASME Cogen-Turbo Power Meeting, Portland, OR, October 25-27, 1994.